Nano Energy 146 (2025) 111488

Contents lists available at ScienceDirect

Nano Energy

journal homepage: www.elsevier.com/locate/nanoen

Triboelectrification during non-wetting liquids intrusion–extrusion in hydrophobic nanoporous silicon monoliths

Luis Bartolomé [a,*,1], Nicola Verziaggi [b,1], Manuel Brinker [c,d], Eder Amayuelas [a], Sebastiano Merchori [b], Mesude Z. Arkan [e], Raivis Eglītis [f], Andris Šutka [f], Mirosław Chorążewski [e], Patrick Huber [c,d], Simone Meloni [b,*], Yaroslav Grosu [a,e,**]

[a] Centre for Cooperative Research on Alternative Energies (CIC energiGUNE), Basque Research and Technology Alliance (BRTA), Alava Technology Park, Albert Einstein 48, Vitoria-Gasteiz 01510, Spain
[b] Dipartimento di Scienze Chimiche, Farmaceutiche e Agrarie, Università degli Studi di Ferrara, Via Luigi Borsari 46, Ferrara I-44121, Italy
[c] Institute for Materials and X-ray Physics, Hamburg University of Technology, Denickestr. 15, Hamburg 21073, Germany
[d] Centre for X-ray and Nano Science CXNS, Deutsches Elektronen-Synchrotron DESY, Notkestr. 85, Hamburg 22607, Germany
[e] Institute of Chemistry, University of Silesia, Katowice 40-006, Poland
[f] Institute of Physics and Materials Science, Faculty of Natural Sciences and Technology, Riga Technical University, P. Valdena Street 3/7, Riga LV-1048, Latvia

ARTICLE INFO

Keywords:
Triboelectric nanogenerators
Intrusion–extrusion
Nanoporous materials
Silicon monolith

ABSTRACT

Triboelectric nanogenerators (TENGs) have emerged as promising devices for converting mechanical energy into electrical energy through contact electrification and electrostatic induction. However, the generated energy, unlike instantaneous power, current and voltage, is rarely addressed in the vibrant research field of TENGs. In this study, we investigate Intrusion–Extrusion Triboelectric Nanogenerators (IE-TENGs) based on nanoporous silicon monoliths and non-wetting liquids (i.e., water and a 1 mg/mL polyethylenimine solution), addressing the energy generated during this process, conversion efficiency as well as the mechanism underlying the observed phenomena. Compared to powder-based IE-TENGs, the use of monolithic silicon structures enables more efficient and reproducible energy harvesting, with significant improvements in both instantaneous power density and energy per cycle. We also analyzed the impact of compression rate and liquid properties on electrical output, showing that higher compression rates improve power generation, while modifying the liquid medium significantly improves conversion efficiency, reaching up to 9 %. Furthermore, through computational analysis, we identify the crucial role of grafting defects on the generated triboelectric output. This work introduces a novel approach to triboelectric energy harvesting by implementing a monolithic nanoporous architecture and offering an alternative pathway for enhancing contact electrification via confined solid–liquid interfaces. These findings provide new insights into the triboelectric behavior of porous systems and pave the way for next-generation high-performance IE-TENGs, with potential applications in wearable electronics, environmental energy harvesting, and self-powered sensing systems.

1. Introduction

The growing demand for sustainable energy solutions has driven extensive research into energy harvesting technologies that can convert ambient mechanical energy into electrical power. These technologies could play a crucial role in diverse applications including power generation, transportation and electronics, requiring multiple strategies to achieve widespread implementation. Among these technologies, triboelectric nanogenerators (TENGs), also known as nanotribogenerators, have emerged as a promising means of harnessing and harvesting mechanical energy from environmental sources such as motion, vibration, and liquid flow [1].

TENGs operate based on the principles of contact electrification and electrostatic induction [2]. While in solid-solid contact electrification,

* Corresponding authors.
** Corresponding author at: Centre for Cooperative Research on Alternative Energies (CIC energiGUNE), Basque Research and Technology Alliance (BRTA), Alava Technology Park, Albert Einstein 48, Vitoria-Gasteiz 01510, Spain.
E-mail addresses: lbartolome@cicenergigune.com (L. Bartolomé), simone.meloni@unife.it (S. Meloni), ygrosu@cicenergigune.com (Y. Grosu).
[1] These authors contributed equally.

https://doi.org/10.1016/j.nanoen.2025.111488
Received 4 June 2025; Received in revised form 3 September 2025; Accepted 27 September 2025
Available online 28 September 2025

the charge transfer mechanism could be attributed to material transfer [3], in the case of solid-liquid contact, there is a steamed discussion on how/whether charge is transferred between two dissimilar materials upon contact and separation [4], as well as the driving forces behind this phenomenon. As a result, a comprehensive understanding of the mechanism is still lacking. Since their first demonstration [5], TENGs have undergone significant advancements, exhibiting high instantaneous power density, scalability, and broad material compatibility [1]. With applications spanning micro/nano power sources, self-powered sensors, blue energy or direct high-voltage power sources, [6] these devices have been successfully integrated into wearable electronics, self-powered sensors, and large-scale energy networks [7]. However, despite their potential, challenges remain in optimizing their charge transfer efficiency, conversion efficiency, long-term stability and integration with existing power systems [8]. Moreover, the amount of generated energy is rarely presented in the literature, focusing more on instantaneous power, voltage and current. While those quantities can reach very high values and are important for practical applications, they do not define conversion efficiency, which is crucial for harvesting technologies.

Since unused or wasted energy can come in many forms, different TENG strategies are required to harvest, harness and convert it effectively and efficiently. One particularly promising approach involves the conversion of solid-liquid interactions into electrical energy, which has gained significant attention offering a potential route for self-powered devices due to its unique advantages [9]. Unlike conventional solid–solid TENGs, solid-liquid TENGs offer self-healing capabilities, adaptability to dynamic environments and improved charge transfer efficiency. Research has demonstrated that material and/or liquid modifications, such as the use of ionic solutions [10,11], conductive polymers [12] or hydrophobic surfaces [13], can significantly enhance the triboelectric output, opening new pathways for energy harvesting in aqueous and biomedical environments [14].

A specific implementation of liquid–solid TENGs is the Intrusion–Extrusion Triboelectric Nanogenerator (IE-TENG) [15–17], which leverages the hydrophobic nanoporous architecture of materials to generate electricity through the controlled movement of liquid into and out of confined spaces. The intrusion–extrusion cycle induces charge accumulation and redistribution, leading to voltage and current fluctuations that can be exploited for energy conversion. A major advantage of IE-TENGs is their ability to overcome a key limitation of traditional TENGs, i.e., restricted contact area between materials in contact. By leveraging nanoporous materials with surface areas reaching hundreds to thousands of square meters per gram, IE-TENGs have the potential to significantly enhance the area-specific energy density and, ultimately, the overall efficiency of triboelectric devices. They also allow for proper calculation of the mechanical energy (and hence conversion efficiency) involved in the conversion cycle, which is often challenging in traditional TENGs [18].

In this work, nanoporous silicon monoliths, a material researched in a wide variety of research fields [19], ranging from medical and biological sciences [20], optics and electronics [21] and mechanical functionalization [22], were investigated as a promising material for IE-TENGs, offering two main advantages. First, conductive (doped) porous silicon enhances charge transfer and collection during the intrusion–extrusion process, improving electrical output efficiency [23]. Second, nanoporous silicon monoliths can be functionalized via grafting to achieve hydrophobic surfaces, which are essential for intrusion–extrusion-based energy generation, while also enhancing triboelectric output through the incorporation of specific functional groups, as demonstrated in various studies [24–26].

By demonstrating a three-order-of-magnitude increase in instantaneous power density and a two-order-of-magnitude increase in energy per intrusion-extrusion cycle, both compared to previous passive (no bias voltage) configurations using powdered porous materials [17], this study establishes porous silicon monoliths as a promising candidate for next-generation IE-TENGs. Additionally, we identify pore size and porous thickness layer, i.e., the overall pore volume, of nanoporous silicon monoliths as the two primary factors governing triboelectric performance. Furthermore, our analysis of the compression/decompression rate during the intrusion–extrusion process and the impact of liquid properties reveals that higher compression rates enhance electrical power generation, while modifying the liquid medium significantly improves triboelectric efficiency. Additionally, through computational analysis combining classical molecular dynamics (MD) with *ab initio* simulations, we successfully reproduced the grafted silica-silicon surface and quantified the charge transfer at the solid-liquid interface. Moreover, by integrating a robust nanoporous silicon monolith structure and combining experimental insights with atomistic simulations, this study offers a unique platform for elucidating and optimizing triboelectric phenomena at the solid–liquid interface, surpassing the constraints of previous powder-based systems [17]. These findings provide a strong foundation for further optimizing solid–liquid triboelectric energy harvesting, paving the way for applications in wearable electronics, environmental energy harvesting, and self-powered sensing systems.

2. Results and discussion

In this work, we explored a passive configuration (Fig. 1a) of IE-TENG to study the triboelectrification output of the nanoporous silicon monoliths, meaning no bias voltage was applied. As demonstrated in our previous research [17], the intrusion and extrusion of water within a hydrophobic matrix are accompanied by electrical energy release (see Supp. Inf. Section 1), offering a novel approach to harnessing mechanical energy through solid-liquid interactions. Specifically, Fig. S1 shows how triboelectrification peaks occur precisely during intrusion and extrusion, while Fig. S2 demonstrates the correlation between intrusion pressure and pore size across the different samples.

During the intrusion, high pressure forces liquid into the hydrophobic nanoporous structure, leading to a significant triboelectric output. Conversely, when the pressure is released, the liquid is allowed to exit the pores (extrusion) also causing triboelectric generation. These processes manifest as sudden spikes in electrical current and voltage signals. These abrupt electrical fluctuations are a direct consequence of variations in the solid-liquid interface, where the interfacial surface expands during intrusion and contracts during extrusion. These peaks are followed by an extended decay in the signal, which is not typically expected in conventional TENG behavior. While the precise mechanism behind this prolonged decay remains under investigation, our simulations suggest that the reversible formation and annihilation of surface defects may significantly contribute to the observed electrification (see Section 5.4). If, as indicated by our simulations, this reversible defect dynamics governs the sustained electrical relaxation following the intrusion–extrusion process, then the associated local charge redistributions and chemical interactions—occurring over timescales that may extend well beyond seconds—could plausibly account for the long decay observed. Although the behavior of intrusion-extrusion accompanied by triboelectrification is not exclusive to nanoporous silicon monoliths, having also been previously reported in our triboelectrification studies involving powdered nanoporous silicas and MOFs [15–17], this work specifically investigates nanoporous silicon monoliths as material for IE-TENGs, aiming to optimize the charge transfer and collection during the intrusion–extrusion process. By utilizing a nanoporous silicon monolith, this approach enhances the collection of the generated triboelectric output due to the conductive nature of the material, reducing power loss during intrusion–extrusion process. Moreover, this configuration is a single-electrode configuration, unlike previously reported double-electrode configurations of IE-TENGs [15–17]. As shown in Fig. 1a, the monolith is located inside the metallic vessel and connected to the circuit, which includes the ammeter and voltmeter, both grounded. To study and optimize charge transfer and collection, the electrical performance of nanoporous silicon monoliths is investigated. As observed in Fig. 1b and c, both current and voltage signals exhibit abrupt changes, which are positive during

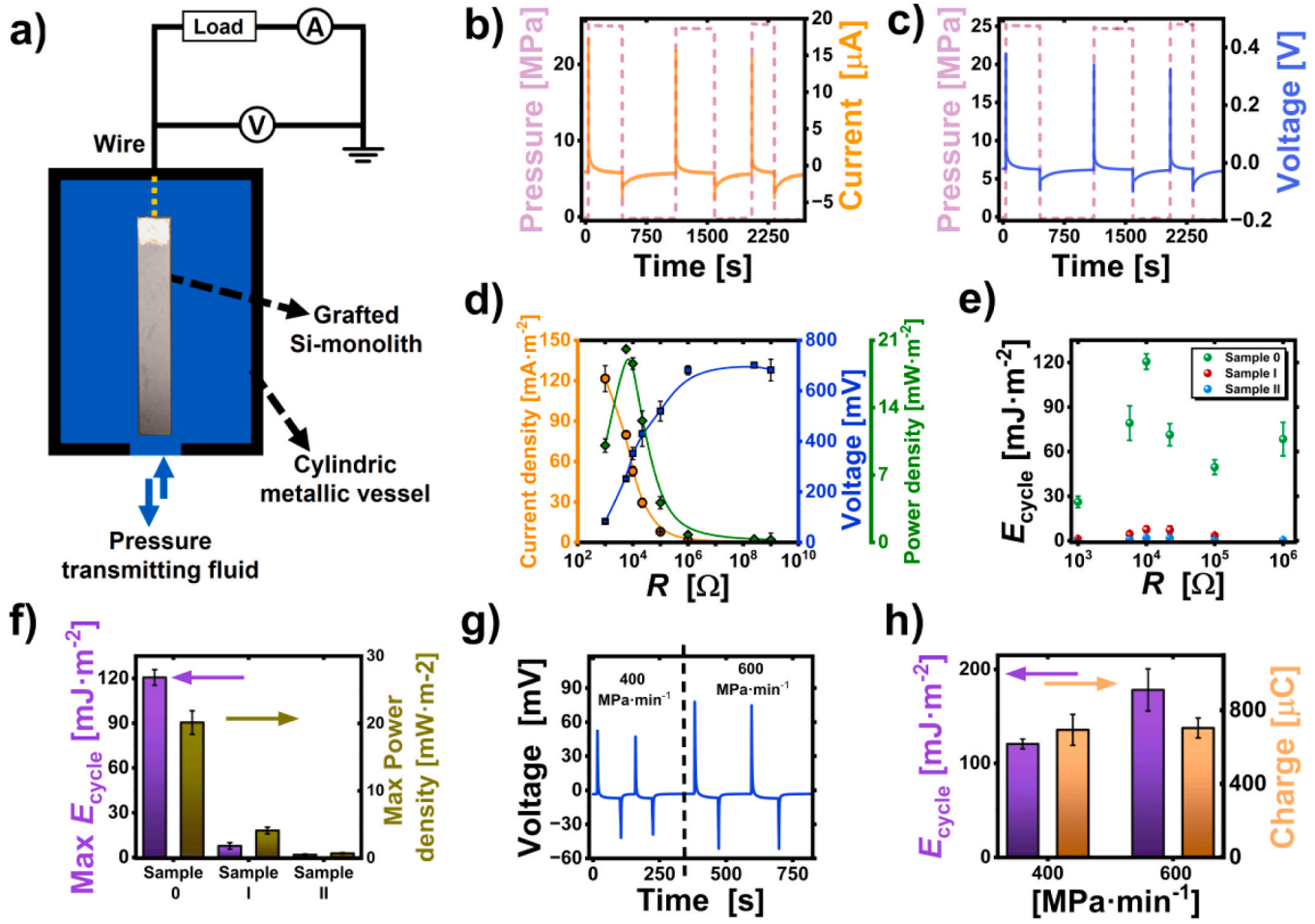

Fig. 1. {Porous silicon monolith + water} IE-TENG tested in the passive single-electrode configuration for triboelectrification. (a) Schematic diagram. (b) Current and (c) voltage during the intrusion–extrusion cycles for sample 0, with a load resistor $R_L = 22$ kΩ. (d) The voltage, current and power output for sample 0 under various external load resistances, with a maximum instantaneous power density of around 10–20 kΩ. (e) Comparison of the energy per cycle for the different samples under various external load resistances. (f) Maximum energy per cycle and instantaneous power density of the tested samples. (g) Voltage during water intrusion–extrusion cycles under different compression/decompression rates, Sample II, $R_L = 22$ kΩ. (h) Energy per intrusion–extrusion cycle and generated charge for compression/decompression rates of 400 MPa min^{-1} and 600 MPa min^{-1}, Sample 0, $R_L = 22$ kΩ.

intrusion and negative during extrusion. These alternating peaks indicate a directional electron flow in the external circuit, with electrons moving toward the silicon monolith during intrusion and flowing away from it during extrusion. These experimental observations suggest that the silicon monolith attracts electrons upon intrusion and donates them during extrusion. In the case of voltage, these alternating peaks may reflect charge accumulation during intrusion due to the increased solid-liquid interfacial contact area and the release of the stored charge during the extrusion. While these phenomena will be further explored through theoretical simulations, Fig. 2 provides a combined perspective, overlaying these experimental findings with theoretical results from simulations to illustrate the charge separation mechanism during intrusion-extrusion when the system is under steady-state cycling conditions, i.e. after several cycles. Based on the convergence of independent experimental and theoretical analyses, we propose a four-stage model describing the charge separation process in IE-TENGs based on nanoporous silicon monoliths.

We examined the triboelectric output across varying load resistances, quantifying both the corresponding instantaneous power density (Fig. 1d) and the energy per intrusion–extrusion cycle (Fig. 1e), see Supp. Inf. Section 2 for the methodology used to calculate these parameters. The results reveal a strong dependence on pore volume and surface area, with sample 0, characterized by the highest porosity, exhibiting the highest instantaneous power density and energy per cycle (Fig. 1f). Given that the triboelectric output scales with the solid–liquid interface, this finding underscores the necessity of highly porous samples to enhance the efficiency of IE-TENGs based on nanoporous silicon monoliths. Note that for the used samples, the porous layer is only 10–33 μm. Further enhancement of porosity is expected to improve the performance (see Fig. 1f and further experiments below).

For sample 0, the instantaneous power density reaches 20 ± 2 mWm^{-2} and the maximum electrical energy per intrusion–extrusion cycle is 121 ± 5 mJ m^{-2}. While these values remain lower than the highest-reported instantaneous power densities in the TENG field, where outputs reaching thousands of watts per square meter have been documented [8,27], we highlight a drastic difference between the obtained results and those previously reported. Typically, TENGs demonstrate high values of voltage and current in a very short period of time, such as milliseconds, which results in a low energy output. While here, power generation occurs for minutes after intrusion or extrusion (see Fig. S1). Therefore, while instantaneous power density is lower due to the slower process of intrusion-extrusion in the performed tests, the generated energy is actually the relevant parameter to access.

To further enhance the performance of IE-TENGs utilizing nanoporous silicon monoliths, we investigated the impact of compression/decompression rate and the liquid in the system, i.e., the liquid which intrudes/extrudes the silicon monolith. These factors are crucial in determining the overall energy conversion efficiency and the practical

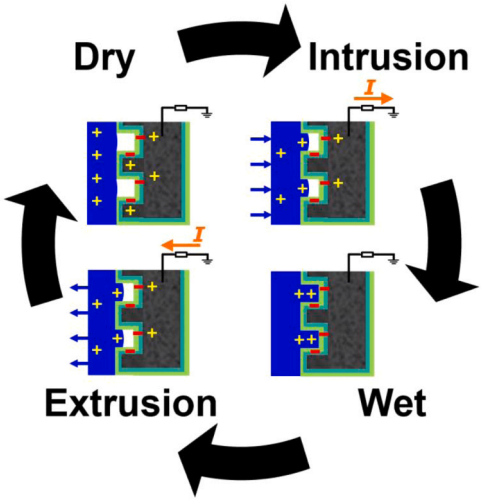

Fig. 2. Scheme of charge separation. Schematic diagram illustrating the proposed four-stage charge separation mechanism in an IE-TENG based on nanoporous silicon monoliths. This mechanism is derived from the convergence of experimental observations and theoretical simulations, highlighting how solid-liquid interfacial changes lead to electron flow. In particular, the diagram outlines how electrons are attracted to the p-doped conducting silicon monolith during intrusion and donated during extrusion, enabling reversible charge transfer. This model visually explains the physical origin of the triboelectric signal generated by the intrusion–extrusion process under steady-state cycling conditions.

applicability of IE-TENGs in energy harvesting. Fig. 1g illustrates that as the compression rate increases, the voltage peaks exhibit a proportional enhancement, a trend consistent with previous studies on IE-TENGs employing powdered materials [17]. Consequently, the electrical energy per cycle also rises with an increase in the compression rate (for further details see Supp. Inf. Section 3). For instance, when the rate is increased from 400 MPa min^{-1} to 600 MPa min^{-1}, the energy per cycle improves by 50 %, increasing from 121 ± 5 mJ m^{-2} to 180 ± 20 mJ m^{-2}. Interestingly, despite the increase in voltage peaks and energy output, the total generated charge remains unchanged (Fig. 1h). This effect is attributed to the fact that the charge transfer capacity is primarily dictated by the contact area and intrinsic material properties of the nanoporous silicon monolith. However, the electrical power output—which, when integrated over time, determines the electrical energy per cycle—is directly affected by the compression rate. This phenomenon occurs due to: i) Charge transfer dynamics, i.e., at higher compression rates, the same amount of charge is transferred over a shorter period, leading to an increase in the current peak magnitude and ii) Electric field enhancement, i.e., in accordance with Maxwell's equations, faster charge redistribution induces greater variations in the electric field, resulting in higher voltage spikes and, consequently, enhanced electrical power generation.

Finally, to explore the influence of the liquid on the output of IE-TENG we conducted a comparative study using water and an aqueous polyethylenimine (PEI) solution (1 mg/mL) with monolith sample V—Fig. 3a. PEI was selected following the triboelectric series [28]. As shown in Fig. 3b, PEI solution exhibited an increase in electrical peak values compared to water, leading to higher overall electrical output (Table 1). As a hypothesis, this enhancement may be attributed to differences in the dielectric properties and ionic composition of the liquids, which modulate the charge transfer performance at the solid–liquid interface. Notably, the PEI solution demonstrated a remarkable improvement in electrical performance, achieving an efficiency of 9 %—calculated as the ratio of electrical energy output to the mechanical work performed during the intrusion–extrusion cycle.

We believe that the notable increase in energy conversion efficiency observed when using the PEI solution can be attributed to both interfacial dielectric effects and the chemical nature of PEI. While the low concentration of PEI means that bulk physicochemical properties such as viscosity and surface tension remain largely similar to those of water [29,30], the dielectric constant is significantly affected even at low concentrations. Our measurements show that the PEI solution (1 mg/mL) has a dielectric constant of ~270, significantly higher than that of water (~80). This increase in permittivity can enhance triboelectric output by allowing more efficient charge separation and storage at the solid–liquid interface. While it might be intuitively expected that a high-permittivity liquid would increase charge screening, we believe that in our system, the PEI solution reduces internal field loss and enables stronger effective electric fields. This leads to a higher quantity of triboelectric charge being generated and transferred. From a capacitive standpoint, a higher dielectric constant increases the capacitance between the contacting surfaces, which allows more charge to accumulate for a given electric potential difference [31]. This is consistent with triboelectric theory, where the surface charge density is positively correlated with the dielectric constant of the medium. Indeed, prior studies confirm that enhancing the dielectric constant in triboelectric layers can lead to significant improvements in output performance [31]. However, the

Table 1
Electrical output with different liquids. Instantaneous power density, electrical energy per intrusion–extrusion cycle and efficiency using different liquids, compression/decompression rate of 600 MPa min^{-1} and R_L= 10 kΩ.

System	Inst. power density [mW m^{-2}]	Energy per cycle [J m^{-2}]	Efficiency [%]
{Porous silicon monolith sample V + H_2O}	1.06 ± 0.08	0.053 ± 0.015	0.06
{Porous silicon monolith sample V + PEI sol.}	68 ± 4	10 ± 1	9

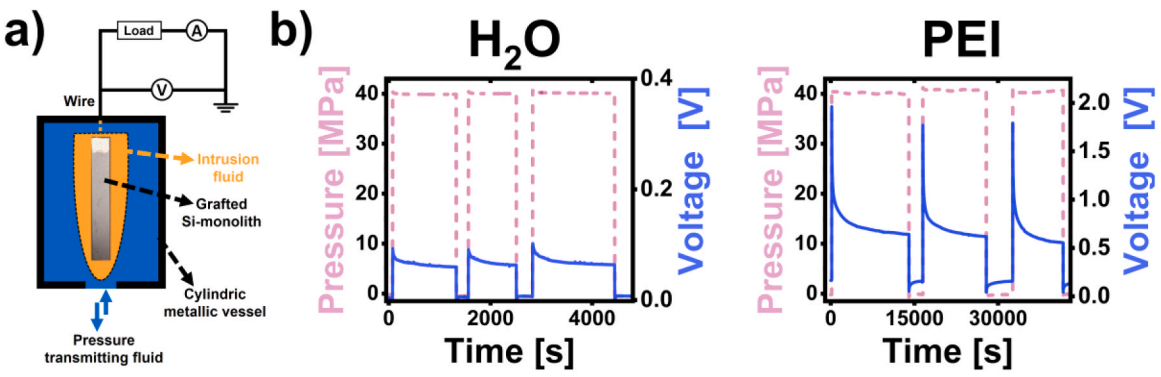

Fig. 3. {Porous silicon monolith sample V + liquid} IE-TENG tested in the passive single-electrode configuration for triboelectrification: (a) Schematic diagram. (b) Voltage during intrusion–extrusion cycles for porous silicon monolith with water (H_2O) and PEI solution (1 mg/1 mL), Sample V, $R_L = 10$ kΩ.

dominant factor likely lies in the molecular structure of PEI, which is rich in amine (–NH_2) functional groups known for their strong electron-donating character. These groups facilitate charge transfer at the interface by readily donating electrons to the solid surface, particularly when the solid material tends to accept electrons, as in the case of fluorinated grafting [32,33]. Consequently, the presence of PEI enhances surface charge density and strengthens the triboelectric signal. This role of PEI in amplifying solid–liquid charge transfer dynamics is also found in studies where PEI layers can significantly lower the work function of electrodes and induce interfacial dipoles in electronic systems, even at low concentrations [34]. Interestingly, the performance enhancement is even more pronounced in the intrusion–extrusion configuration. Comparing water and the PEI solution, we observe a ~2× voltage improvement in immersion experiments (see Supp. Inf. Section 4) but nearly a ~10× improvement in the dynamic intrusion–extrusion tests (Fig. 3). This suggests an additional mechanism at play. Our proposed triboelectrification mechanism centers on charge transfer occurring at defect sites in the fluorinated grafting layer (see below). Given PEI's amphiphilic nature, comprising both hydrophilic amine groups and hydrophobic hydrocarbon chains, it can interact with polar water and simultaneously adsorb onto the hydrophobic (–CF_2–) grafted surfaces. We hypothesize that PEI selectively deposits at sites of grafting imperfection, locally disturbing the ordered layer and increasing the number or activity of defect sites. Moreover, PEI's strong electron-donating amine groups can donate electrons to electron-deficient fluorinated defect regions, resulting in negatively charged $(CF_2)_n^-$ sites. The positively charged protonated PEI chains can then electrostatically stabilize these charges, preventing rapid recombination or neutralization. In this way, PEI acts not only as a donor but also as a charge-stabilizing agent, enhancing the triboelectric output by amplifying the effectiveness of the existing surface defects. This synergistic behavior aligns with our broader findings that surface defects are crucial to triboelectric signal generation. The significantly stronger triboelectric response in the presence of PEI is therefore attributed to a combination of its high dielectric constant and its unique chemical and interfacial behavior. Finally, we achieved a 9 % energy conversion efficiency (Table 1), i.e., 9 % of the mechanical energy input was transformed into electric energy output, the latter obtained by integrating power over time, rather than relying on instantaneous values as is often reported in the literature. From this perspective, the results represent a significant advancement in the field of TENGs, even before any broad optimization across different liquid media has been conducted. Comparing energy conversion efficiencies across TENG systems is inherently challenging, as different studies adopt varied assumptions to estimate mechanical input energy. For example, Tang et al. [35] reported an efficiency of 70 %, which includes buoyancy and surface tension, but excludes gravity and damping losses. Yang et al. [36] considered kinetic and potential energy contributions, reaching ~60 %. Wu et al. [37] used gravitational energy from water droplets under idealized conditions to report ~11 %, while Liu et al. [38] estimated ~1 % efficiency from bubble collapse, noting common underestimations of realistic inputs. Even in some studies, if the separation force is not considered, the efficiency could be longer than 100 % [18]. Therefore, because efficiency strongly depends on how both input and output energies are defined, we emphasize that direct comparisons require careful standardization.

The mechanism of contact electrification is very complex and remains unclear. This is particularly enhanced when organic grafting and polymeric solutions are involved. For this reason, we decided to compare how the effect of PEI on intrusion-extrusion electrification compares with more common solid-liquid electrification configurations, such as solid-liquid immersion-emersion TENG and droplets electrification experiments. Fig. S6 in Supp. Inf. Section 4 indicates that the electrification enhancement of PEI solution compared to water is also evident in immersion-emersion tests performed for the grafted silicon monolith. However, it can be seen that the enhancement is not as dramatic as for the intrusion-extrusion process. While the signals from intrusion–extrusion and immersion–emersion exhibit qualitative similarities, they differ quantitatively, suggesting that the underlying charge transfer dynamics are not fully equivalent. In contrast, the response observed in the droplet experiments (Fig. S7) differs significantly in both magnitude and character, indicating the presence of a distinct triboelectric mechanism that is not comparable to those governing intrusion-extrusion and immersion-emersion. Detailed interpretation of the droplet experiment is outside the scope of the current work and will be discussed elsewhere.

To further enhance the efficiency of IE-TENGs, the strategy of increasing the triboelectric contact area of TENGs using nanoporous materials remains highly promising, presenting exciting challenges that must be addressed for future advancements. Beyond efficiency, the use of nanoporous conductive materials introduces a key technological advantage: fast charge kinetics. The ability of the nanoporous silicon monoliths to serve as both the triboelectric active material and the electrode significantly accelerates charge relaxation, reducing the time required for voltage and current recovery after an intrusion or extrusion event. This property is highly desirable for high-frequency energy harvesting systems, particularly in applications involving vibrational energy scavenging, such as self-powered sensors in industrial machinery or wearable devices [39].

3. Results of the simulation of silicon monoliths for IE-TENGs

In this study, we employ simulations to identify the microscopic origin of the triboelectrification mechanism in the monolith configuration. Due to the inherent differences in spatial and temporal scales between simulations and experiments, a quantitative prediction of the electrical characteristics of the device using quantum mechanics simulations is not feasible. Therefore, our focus is placed on elucidating the qualitative aspects that govern the process. In particular, we investigated the interplay between structural defects, chain orientation, and electronic charge distribution between the various layers of the solid and the liquid upon intrusion/extrusion. Building on our previous work on triboelectrification of grafted silica powder [17], grafted defects may play a crucial role in the process. Consistently, we examined three variants of the system. The grafting defect-free case, where all the chains remain covalently bonded to the silica surface and, additionally, we also considered two grafting defected cases, where the bond between one chain and the SiO_2 slab was broken. This breaking can be obtained in two different ways, leaving Si^+ on the silica surface (denoted Si-defect in the following), while producing a $(C8\text{-}CF_3O)^-$ defected chain, or the complementary case of a O^- defect (denoted O-defect in the following) on the SiO_2 surface and the formation of a complementary $(C8\text{-}CF_3Si)^+$ defected chain. In this work, we do not investigate whether the grafting defects of either type are formed during intrusion–extrusion, we simply analyze the consequences of the possible presence of grafting defects. In our previous work on grafted silica powder [17], we have already shown how the formation of grafting defects is crucial to explain the experimental differences between C8-CF_3 grafting and the hydrogenated counterpart.

Under intrusion conditions, where water is in very close contact with the grafted silica, both the $(C8\text{-}CF_3Si)^+$ and $(C8\text{-}CF_3O)^-$ are immediately solvated, as well as Si- and O-defects. This hydration stabilizes the charged species, bringing to the orientation of the defective chains toward bulk water. This configuration maximizes the hydrogen bond or polar interaction (depending on the type of defect) between the defective chains and the liquid while allowing a strong interaction between the hydrophobic ends of defective and non-defective chains (Fig. 4a). On the other hand, under extrusion conditions (in the simulations, when separated from the surface), the absence of solvation, hence lack of electrostatic screen, induces defected chain reorientation toward the complementary Si- or O-defect (Fig. 4b). Upon the macroscopic experimental timescale, this reorientation may result in *defect recombination*, leading to the formation of a covalent bond. In other words, intrusion-extrusion may result in the dynamic formation/annihilation of grafting defects. To test this possibility, an *ab initio* geometry optimization of

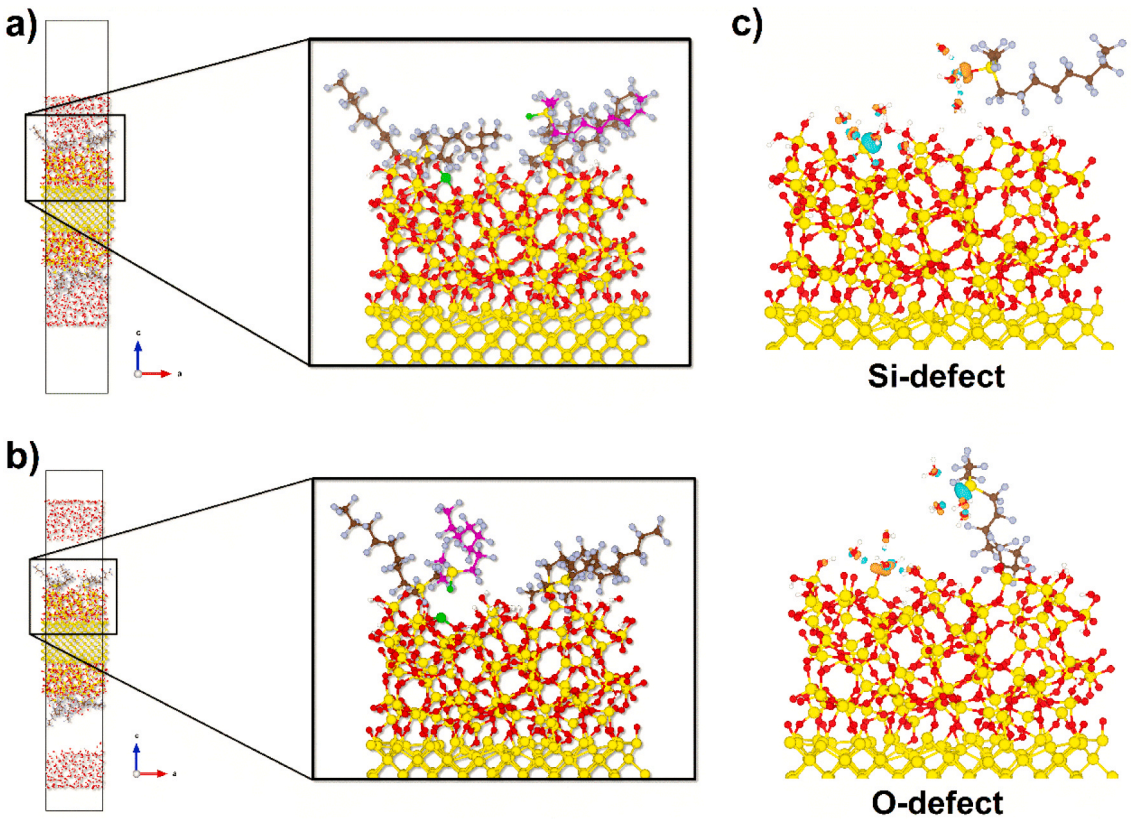

Fig. 4. Computational study of monolith surface when a Si^+ surface defect is created. Atoms in green correspond to the atoms in the defect, i.e., after the bond between silicon and oxygen has been removed, and atoms in magenta are the carbons of the detached chain, (a) for the intruded case where, for better visualisation, all water molecules in contact with the surface have been removed, and (b) for the extruded case. Difference in charge density between the total system and the individual solid and water components $\Delta\rho = \rho_{\text{total}} - (\rho_{\text{solid}} + \rho_{\text{water}})$. (c) This representation shows how the system distributes the charge once the water is in contact with the solid. In the section shown, only the chains and water molecules involved in the solvation process are highlighted. In light blue, $\Delta\rho < 0$, i.e., the areas where electrons are depleted; in orange, areas enriched with electrons.

the extruded system was performed, where only the defective chain was allowed to move. At the end of the geometry optimization, the covalent bond between the defective chain and the complementary Si- or O-defect was restored, eliminating any local charging associated with the presence of defects. Of course, in systems of experimental size, where defective chains in the solvated state upon intrusion have time and room to diffuse far away from the complementary surface defect, recombination is a slower process.

We now turn to a quantitative analysis of intrusion–extrusion process on the tribocharging of the system. Building on our previous work [17], where the Si-defect system exhibited a stronger effect on the charge separation process, we initially focused our analysis on this configuration. Later in the manuscript, we extended our investigation to the O-defect and defect-free systems to explore possible differences in charge redistribution. Our quantitative analysis is based on the Bader charges [40,41] (see Section 5.4) which provides quantitative insight into the phenomena discussed above and explains the experimental evidence that an outgoing electric current is observed upon intrusion, and *vice versa*. In the Si-defect system, upon intrusion, we observed a charge variation of $-0.67e$ on the defective Silicon atom, indicating that during the intrusion process, the nominally $+1$e Si^+ atom effectively gains electronic charge. This does not imply that upon intrusion the defective silicon became negative. Indeed, as shown in Fig. 4c, it remains positive, but its charge is diminished by -0.67e. We also observe a significant negative charging of the liquid, $-0.36e$. This charge redistribution does not originate from a single source. Still, remarkably, we observed a (total) charge variation of $+0.17e$ within the silicon layer. In other words, upon intrusion, the presence of a surface Si^+ defect induces a polarization effect that extends beyond the immediate silica surface atoms around it, affecting the overall charge distribution, including within the bulk silicon itself.

Importantly, in our simulations, where the system is isolated and electrons cannot be supplied from an external source, intrusion induces only a sizable polarization of the system. However, in an experimental condition, where the system is grounded through the wiring of the (p-doped) silicon layer, the positive charging of this slab drives an electron flux from the external source (the ground) toward the monolith. Considering the convention that positive current flows opposite to the electron flow, simulations predict an outgoing current upon intrusion, which aligns with the experimentally observed current direction. Defective chain reorientation and/or defect annihilation upon extrusion effectively removes the polarization previously induced by the intrusion. This results in a net-zero charging of the Si layer, and a current flux in the opposite direction with respect to intrusion. Within this picture, p-doping of Silicon makes it conductive, allowing the net flux of electrons from the ground to the monolith during intrusion and *vice versa* during extrusion.

Performing the same analysis for the O-defect system, we observed similar behavior. Also in this case, some charge polarization is observed in the system upon intrusion, e.g., a $+0.35$e charging of the nominal surface O-defect. More importantly, the same as in the case of the Si-defected system, upon intrusion, the Si layer gets positively charged. This might be responsible for an electron flow from the ground to the monolith, hence a current in the opposite direction. Remarkably, for the undefective system, no significant charge difference is observed in the silicon layer between the intruded and the extruded states, with charge variation observed only in the other layers (see Table 2). The comparison between the findings for the defected grafting and defect-free systems suggests that the formation of surface defects, both at Si and O sites, is

Table 2
Barder charge differences calculated as $\Delta q_{\text{intrusion}} = q_{\text{intruded}} - q_{\text{extruded}}$.

Intrusion	Defect-free	Si-defect	O-defect
C8-CF_3	0.41	0.45	0.50
SiO_2	−0.04	−0.27	−0.19
H_2O	−0.36	−0.36	−0.46
Silicon-layer	0.00	0.17	0.16
Boron	0.00	0.00	0.00

fundamental to the triboelectrification process. It is only through these defects that we can observe and quantify the polarization of the monolith, making them essential for the overall charge redistribution process.

To qualitatively connect our findings on the monolith with our previous study on the powder-based systems [17], and to propose possible hypotheses for the improved efficiency observed in the monolith setup, we extended our analysis of charge redistribution Δq between the intrusion and extrusion states, as described above. In this analysis, we focus on the Si-defect scenario in the C8-CF_3/SiO_2 system without the underlying silicon slab [17], thereby mimicking the "powder-like" system. In this case, Δq accompanying intrusion is entirely localized on the defective fluorinated chain (C8-CF_3O)$^-$, $\Delta q = +0.55$q, while the corresponding charge loss in water is –0.55q. No significant charge redistribution is observed within the silica layer. Due to the broken symmetry in the system, where C8-CF_3/SiO_2 powder grains accumulate near one of the electrodes, the local polarization between water and the grafted silica grains accompanying intrusion, and the opposite process during extrusion, produces an electric field that drives electrons into and out of the electrodes. As a result, any electrical signal detected at an external metal electrode originates solely from local contact-induced polarization via interaction with individual nanoparticles. In contrast, the monolithic system, which includes the silicon substrate, enables polarization to occur directly within the Si-doped charge collector. Therefore, even if the overall charge separation appears smaller in the monolith, its key advantage lies in enabling direct polarization within the electrode, contributing to improved energy conversion efficiency.

4. Conclusions

This work presents a study on the use of nanoporous silicon monoliths for Intrusion–Extrusion Triboelectric Nanogenerators (IE-TENGs), demonstrating their superior performance over powdered porous materials in triboelectric energy harvesting. By utilizing conductive and porous material, we significantly enhance charge transfer efficiency, leading to higher instantaneous power density and improved energy conversion per cycle. Our results show that pore size and porous layer thickness are key parameters governing triboelectric performance, highlighting the importance of optimizing these structural properties.

Additionally, we found that increasing the compression rate enhances electrical output, while liquid selection plays a critical role in optimizing triboelectric efficiency. In particular, the use of polyethylenimine (PEI) 0.1 % solution leads to a substantial increase in energy conversion efficiency, reaching 9 %, which is among the highest reported for solid-liquid TENGs.

Furthermore, the computational simulations and Bader charge analysis not only provided insight into charging upon intrusion–extrusion but also allowed to identify the crucial role of the grafting defects on generated triboelectric current. By quantifying charge redistribution within the system, we can confirm that the direction of the experimentally observed current aligns with theoretical predictions associated with the presence of a Si-defect on the SiO_2 surface.

Future research should focus on further tailoring pore architectures and surface modifications of silicon monoliths, as well as the liquid selection of the system to optimize the electrical performance of IE-TENG. With continued advancements, IE-TENGs leveraging porous conductive materials could emerge as a viable alternative for high-performance, self-sustaining energy harvesting systems in both wearable electronics and industrial energy recovery applications.

5. Methods and materials

5.1. Materials

The hydrophobic nanoporous silicon monoliths (Fig. 5a) used in this work were produced by the following protocol (Fig. 5b). First, porous silicon was synthesized in an electrochemical etching procedure from p-doped single-crystalline silicon wafers (resistivity 0.01–0.02 Ω·cm, (100) orientation, 525 ± 25 μm thickness, single-side polished). The silicon wafer was installed in an electrochemical cell, which was filled with a 2:3 volumetric mixture of hydrofluoric acid and ethanol (absolute) and a current was applied between a platinum counter electrode

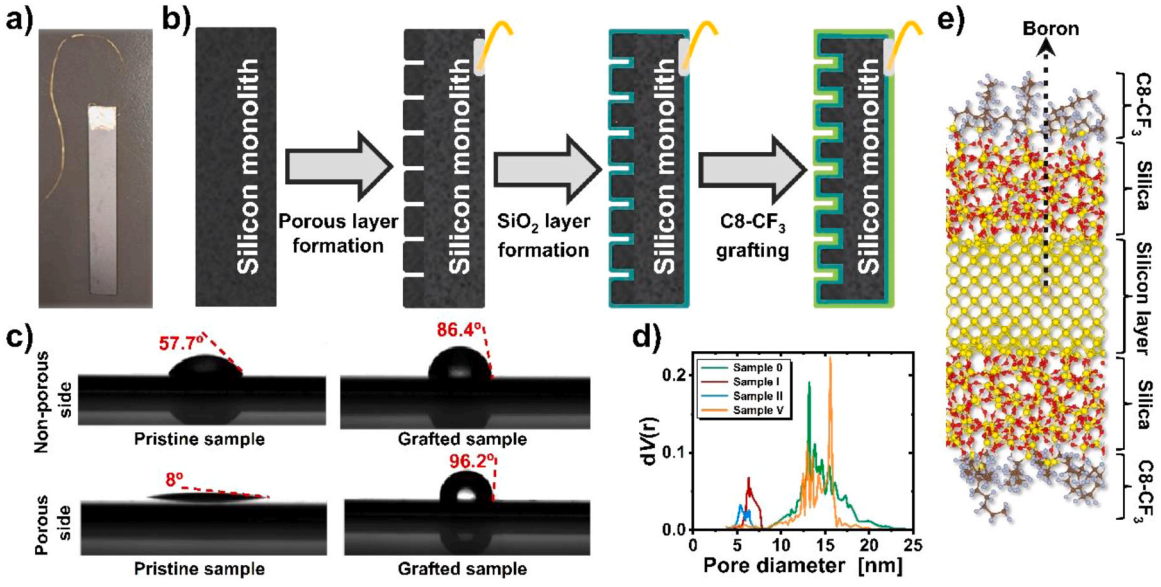

Fig. 5. Silicon monolith samples. (a) Scheme of the production protocol followed for the nanoporous silicon monolith samples. (b) Silicon monolith sample where a gold wire attached with conductive silver epoxy can be observed. (c) Contact angles of non-porous and porous sides of samples before and after grafting to obtain a hydrophobic surface. (d) Pore size distribution of the samples used in the triboelectrification tests. (e) Computational model of grafted silicon monolith.

Table 3
Properties of nanoporous silicon monolith samples. Textural and surface properties from gas adsorption, along with sample size and configuration of silicon monoliths used in triboelectrification tests.

Sample	Pore size Ø [nm]	Porous layer thickness [μm]	Configuration	Sample Area [cm^2]	Pore volume [cm^3]
0	13.2	33.1	Single-side	6.69	0.014
I	6.2	14.5	Single-side	6.87	0.006
II	4.8	10	Single-side	6.51	0.004
V	15.4	31.8	Double-side	3.17	0.0086

and the wafer. To obtain porous silicon layers with different pore size and porosity, the current density was varied from 80 mA cm^{-2} to 25 mA cm^{-2} and to 12.5 mA cm^{-2}, for samples 0, I and II, respectively. The current was applied for 10 min for all samples. The values of both pore size and the porous layer thickness for the samples used in this work are summarized in Table 3. After this first step, a SiO_2 layer of around 1 nm is synthesized on the silicon pore surface by immersing the porous silicon samples in H_2O_2 for 20 h. To obtain hydrophobicity (Fig. 5c), the monolith was vacuum-dried overnight at 120 °C, then immersed in a 1.1 M ethanolic ammonia solution at 50 °C and stirred for 30 min. Grafting with fluorinated C8 alkyl silane 1H,1H,2H,2H-perfluorooctyltrichloroxsilane (PFOTCS) was performed by adding it dropwise in excess (5 molecules·nm^{-2} of porous surface), followed by stirring for 120 h. After 5 days, the monolith was rinsed three times with ethanol and dried overnight at 70 °C. This grafting approach was chosen due to its demonstrated pronounced triboelectrification effects with water [17,32]. The contact angle for water wetting was determined using the sessile drop technique conducted by LAUDA Surface Analyzer LSA 100 (LAUDA Scientific GmbH) using the software SurfaceMeter.

Sample V was designed to have a similar pore size and porous layer thickness as Sample 0 (Table 3) but shorter and with a double-sided configuration, in which two porous silicon segments were joined using silver epoxy at their non-porous sides.

The tested liquids were distilled water and an aqueous polyethylenimine (PEI) Solution (1 mg/mL, Sigma-Aldrich, CAS: 9002–98–6).

5.2. PVT-device

The triboelectrification tests were conducted using a high-pressure variable volume unit (HPVV-800), custom-made by Eurotechnica and later modified at CIC energiGUNE. This setup is described in detail in previous work [17]. A brief description is given below. This unit comprises a piston drive module (XL NEMESYS) and a high-pressure steel syringe (10 mL), both supplied by CETONI. The system operates at a maximum pressure of 80 MPa. The drive module is controlled via QmixElements software, which precisely measures and logs pressure (±0.1 kPa), volume variation (±0.01 μL), and temperature (±0.01 K) within the cell.

For testing, the syringe body was directly connected to a cylindrical stainless steel 304 L vessel (Ø 20 mm, length 80 mm), where the samples were placed. This vessel, along with its connections, was designed and custom-built at CIC energiGUNE. For additional details, see Supp. Inf. Section 5. Water was used as the pressure-transmitting fluid in all triboelectrification tests. The nanoporous silicon monolith samples were positioned inside the vessel, with a gold wire attached to them using conductive silver paste (Fig. 5a). This gold wire was then connected to the circuit via additional wiring (Fig. S8), which passed through a custom-built lid that sealed the vessel.

5.3. Material characterization

The textural properties of the samples were characterized using a Quantachrome Autosorb iQ automated gas adsorption instrument. After outgassing the samples at 180 ºC under vacuum for 20 h, nitrogen physisorption isotherms were measured at the temperature of liquid nitrogen (-196 °C). The textural and surface properties of the samples were determined using the BET equation [42,43], following the linearization method proposed by Parra et al. [44] The pore size distribution (Fig. 5d) was estimated by applying the Barrett-Joyner-Halenda (BJH) model to the desorption isotherm branch [45]. Total pore volume was calculated as the volume of gas adsorbed at a relative pressure of 0.99, expressed in $cm^3 \cdot g^{-1}$, using the density of liquid nitrogen to convert the amount of gas adsorbed in STP conditions with the equation $V_{(\text{total pores})}$ ($cm^3 \cdot g^{-1}$)=$V_{(\text{gas adsorbed})}$ ($cm^3 \cdot g^{-1}$, STP)× 0.00154643. The gas adsorption characterization of samples is summarized in Table 3.

5.4. Theoretical approach: simulations and calculations

Building on our previous hierarchical approach [17], where classical MD simulations were seamlessly integrated with *ab initio* analyses to sample configurations and track electron transfer routes, we have developed a computational framework that extends our understanding of the interfacial phenomena in the grafted monolith system. The computational model of sample consists of a ~15 Å silicon layer, symmetrically enclosed within two ~12 Å-thick SiO_2 layers, forming a sandwich-like structure. The silicon layer was p-doped with boron atoms, corresponding to a doping concentration of ~0.3 % (one boron atom among the 384 silicon atoms), to accurately replicate the experimental sample doping. Additionally, the silica layer was functionalized with C8-CF_3 terminal chains, at a grafting density of 1.055 chains nm^{-2} (Fig. 5e), closely matching the experimental grafting. As in our previous study, we examined both a defect-free system and a grafting-defected system. For the latter, we considered two defect scenarios; (i)a case where Si-O bond between a grafting molecule and the silica surface is broken, leaving a Si^+ site on the silica surface while forming a $(C8\text{-}CF_3O)^-$ defected chain and (ii)a complementary case where an O^- defect forms on the surface, leading to the creation of a $(C8\text{-}CF_3Si)^+$ defect chain.

The objective of this theoretical investigation is to identify the mechanism responsible for the electric current measured during intrusion–extrusion process. Thus, to achieve this, we analyzed the changes in system characteristics when in contact with water (512 molecules) and when water is absent, representing the system at the end of intrusion and at the end of extrusion, respectively. Particularly, to mimic experimental conditions, a 25 MPa compression was applied to the system for the intruded state of the model. Conversely, for the extruded state, water molecules were displaced 15 Å away from the surface on both sides of the model. Both states were equilibrated and subsequently simulated using classical MD at 300 K for a total of 11 ns, ensuring sufficient sampling of the interface system.

Classical MD simulations were performed using the LAMMPS package [46,47], employing well-established force fields to parameterize the different components of the system [17]. The Emami et al. [48] force field was used to describe the hydroxylated amorphous silica, while grafted C8-CF_3 chains were modeled using standard OPLS-AA parameters [49] to capture their intermolecular interactions. Moreover, as in our previous work on triboelectrification with powdered grafted silica [17], bonded interactions between the C8-CF_3 chains and the silica surface required *ab initio* calculations to refine some interaction parameters not available in the literature. Finally, water was described by the TIP4P/2005 model [50], which was selected for its ability to accurately represent hydrogen bonding and bulk-phase liquid properties, and Lennard-Jones cross interactions between the liquid and grafted silica were set following the Lorentz-Berthelot mixing rules. Given the high rigidity of silicon compared to the rest of the system, the Si-slab and thin SiO_2 layer on both sides were kept fixed at the geometry obtained from an *ab initio* optimization of the silicon/silica interface. Only the remaining SiO_2 layers, grafted C8-CF_3 chains and water molecules were allowed to move during MD simulations, ensuring their thermal

fluctuations and interfacial interactions were captured under pressure and temperature mimicking experimental conditions. As an extension of our previous framework study [17], this hierarchical approach allows for efficient equilibration and sampling of interfacial structures. Thus, it can be used in *ab initio* electronic structure analyses to investigate the electronic structure of the system upon intrusion–extrusion.

For each intruded and extruded state, with and without grafting defect, five representative configurations were extracted from classical MD simulations at 1 ns intervals to ensure sufficient decorrelation. To analyze the electronic structure, Density Functional Theory (DFT) calculations were performed on these configurations, and the relevant properties were averaged over the five configurations for each system state. DFT calculations were carried out using the Vienna *Ab initio* Simulation Package (Vasp 6.4.0) [51,52] employing the Projector-Augmented Wave (PAW) [53] method along with the Perdew-Burke-Ernzerhof (PBE) [54] exchange-correlation functional. A plane-wave basis set was used to expand the Kohn-Sham orbitals with a kinetic energy cutoff of 400 eV. For convergence criteria, the self-consistent field (SCF) cycle was iterated until the total energy variation between consecutive steps was equal or less than 1.0×10^{-5} eV, ensuring numerical stability in the calculations. Given the complexity of the system, the electronic structure analysis was based on the so-called Bader charge, which determines how the electronic charge is distributed among the different atoms in the system for each considered state. In practice, the total electronic density was first analyzed to identify maxima in the $\rho(x)$ field. The space was partitioned into domains, each assigned to the nearest atomic nucleus. The electronic charge within each domain was then computed and attributed to the corresponding closest atom, ultimately enabling an effective charge analysis for all atoms in the sample.

CRediT authorship contribution statement

Patrick Huber: Writing – review & editing, Supervision, Funding acquisition. **Andris Šutka:** Writing – review & editing, Funding acquisition. **Mirosław Chorążewski:** Writing – review & editing, Supervision, Funding acquisition. **Nicola Verziaggi:** Writing – original draft, Visualization, Methodology, Investigation, Formal analysis, Data curation. **Manuel Brinker:** Writing – review & editing, Investigation. **Simone Meloni:** Writing – review & editing, Supervision, Funding acquisition, Conceptualization. **Luis Bartolomé:** Writing – original draft, Visualization, Methodology, Investigation, Formal analysis, Data curation. **Yaroslav Grosu:** Writing – review & editing, Supervision, Funding acquisition, Conceptualization. **Mesude Z. Arkan:** Writing – review & editing, Investigation. **Raivis Eglītis:** Writing – review & editing, Investigation. **Eder Amayuelas:** Writing – review & editing, Investigation. **Sebastiano Merchori:** Writing – review & editing, Investigation.

Funding

This project leading to this application has received funding from the European Union's Horizon 2020 Research and Innovation Programme under grant agreement No 101017858 and under grant agreement No 964524 EHAWEDRY: "Energy harvesting via wetting-drying cycles with nanoporous electrodes" (H2020-FETOPEN-1-2021-2025). This article is part of the grant RYC2021-032445-I funded by MICIN/AEI/10.13039/501100011033 and by the European Union NextGenerationEU/PRTR. This research received financial support based on Decision No. 2021/43/D/ST5/00062 from the National Science Center (Poland). AŠ acknowledges funding by the Central Finance and Contracting Agency under contract 1.1.1.5/2/24/A/007, ERC Project TriboCharge: "Controlling and exploiting triboelectric effect in polymers for mechanical-to-electrical-chemical conversion". S.M. and A.L.D. acknowledge PRACE for awarding us access to Marconi100 at CINECA, Italy. M.B. and P.H. acknowledge funding by the Deutsche Forschungsgemeinschaft (DFG, German Research Foundation) as part of the Excellence Strategy of the Federal Government and the federal states – EXC 3120/1 – 533771286. M.B. and P.H. also acknowledge the scientific exchange and support of the Centre for Molecular Water Science CMWS, Hamburg (Germany).

Declaration of Competing interest

The authors declare that they have no known competing financial interests or personal relationships that could have appeared to influence the work reported in this paper.

Appendix A. Supporting information

Supplementary data associated with this article can be found in the online version at doi:10.1016/j.nanoen.2025.111488.

Data availability

Data will be made available on request.

References

[1] D. Choi, Y. Lee, Z.H. Lin, S. Cho, M. Kim, C.K. Ao, S. Soh, C. Sohn, C.K. Jeong, J. Lee, M. Lee, S. Lee, J. Ryu, P. Parashar, Y. Cho, J. Ahn, I.D. Kim, F. Jiang, P. S. Lee, G. Khandelwal, S.J. Kim, H.S. Kim, H.C. Song, M. Kim, J. Nah, W. Kim, H. G. Menge, Y.T. Park, W. Xu, J. Hao, H. Park, J.H. Lee, D.M. Lee, S.W. Kim, J. Y. Park, H. Zhang, Y. Zi, R. Guo, J. Cheng, Z. Yang, Y. Xie, S. Lee, J. Chung, I.K. Oh, J.S. Kim, T. Cheng, Q. Gao, G. Cheng, G. Gu, M. Shim, J. Jung, C. Yun, C. Zhang, G. Liu, Y. Chen, S. Kim, X. Chen, J. Hu, X. Pu, Z.H. Guo, X. Wang, J. Chen, X. Xiao, X. Xie, M. Jarin, H. Zhang, Y.C. Lai, T. He, H. Kim, I. Park, J. Ahn, N.D. Huynh, Y. Yang, Z.L. Wang, J.M. Baik, D. Choi, Recent advances in triboelectric nanogenerators: from technological progress to commercial applications, ACS Nano 17 (2023), https://doi.org/10.1021/acsnano.2c12458.

[2] C. Bao Han, W. Du, C. Zhang, W. Tang, L. Zhang, Z. Lin Wang, Harvesting energy from automobile brake in contact and non-contact mode by conjunction of triboelectrication and electrostatic-induction processes, Nano Energy 6 (2014) 59–65, https://doi.org/10.1016/j.nanoen.2014.03.009.

[3] A. Šutka, L. Lapčinskis, D. He, H. Kim, J.D. Berry, J. Bai, M. Knite, A.V. Ellis, C. K. Jeong, P.C. Sherrell, Engineering polymer interfaces: a review toward controlling triboelectric surface charge, Adv. Mater. Interfaces 10 (2023) 2300323, https://doi.org/10.1002/admi.202300323.

[4] Z.L. Wang, From contact electrification to triboelectric nanogenerators, Rep. Prog. Phys. 84 (2021) 096502, https://doi.org/10.1088/1361-6633/ac0a50.

[5] Z.L. Wang, Self-powered nanosensors and nanosystems, Adv. Mater. 24 (2012) 280–285, https://doi.org/10.1002/adma.201102958.

[6] J. Luo, Z.L. Wang, Recent progress of triboelectric nanogenerators: from fundamental theory to practical applications, EcoMat 2 (2020), https://doi.org/10.1002/eom2.12059.

[7] N. Zhang, C. Tao, X. Fan, J. Chen, Progress in triboelectric nanogenerators as self-powered smart sensors, J. Mater. Res. 32 (2017) 1628–1646, https://doi.org/10.1557/jmr.2017.162.

[8] W. Akram, Q. Chen, G. Xia, J. Fang, A review of single electrode triboelectric nanogenerators, Nano Energy 106 (2023) 108043, https://doi.org/10.1016/j.nanoen.2022.108043.

[9] Z. Lin, G. Cheng, L. Lin, S. Lee, Z.L. Wang, Water–solid surface contact electrification and its use for harvesting liquid-wave energy, Angew. Chem. Int. Ed. 52 (2013) 12545–12549, https://doi.org/10.1002/anie.201307249.

[10] D.L. Vu, C.P. Vo, C.D. Le, K.K. Ahn, Enhancing the output performance of fluid-based triboelectric nanogenerator by using poly(vinylidene fluoride-co-hexafluoropropylene)/ionic liquid nanoporous membrane, Int. J. Energy Res. 45 (2021), https://doi.org/10.1002/er.6428.

[11] P. Nellepalli, T. Patel, M.P. Kim, J. Park, Z. Ye, H.W. Jung, H. Ko, J.K. Oh, Self-healable triboelectric nanogenerators based on ionic poly(hindered urea) network materials cross-linked with fluorinated block copolymers, Polym. Chem. 13 (2022), https://doi.org/10.1039/d2py00252c.

[12] L. Wang, W. Li, Y. Song, W. Xu, Y. Jin, C. Zhang, Z. Wang, Monolithic integrated flexible yet robust Droplet-Based electricity generator, Adv. Funct. Mater. 32 (2022), https://doi.org/10.1002/adfm.202206705.

[13] X. Wu, X. Li, J. Ping, Y. Ying, Recent advances in water-driven triboelectric nanogenerators based on hydrophobic interfaces, Nano Energy 90 (2021) 106592, https://doi.org/10.1016/j.nanoen.2021.106592.

[14] W. Xu, Q. Chen, Q. Ren, J. Li, Q. Chen, C. Zhu, Y. Xie, W. Li, Recent advances in enhancing the output performance of liquid-solid triboelectric nanogenerator (L-S TENG): mechanisms, materials, and structures, Nano Energy 131 (2024) 110191, https://doi.org/10.1016/j.nanoen.2024.110191.

[15] Y. Grosu, M. Mierzwa, V.A. Eroshenko, S. Pawlus, M. Chorążewski, J.-M. Nedelec, J.-P.E. Grolier, Mechanical, thermal, and electrical energy storage in a single working body: electrification and thermal effects upon pressure-induced water

intrusion–extrusion in nanoporous solids, ACS Appl. Mater. Interfaces 9 (2017) 7044–7049, https://doi.org/10.1021/acsami.6b14422.
[16] A. Lowe, N. Tsyrin, M. Chorążewski, P. Zajdel, M. Mierzwa, J.B. Leão, M. Bleuel, T. Feng, D. Luo, M. Li, D. Li, V. Stoudenets, S. Pawlus, A. Faik, Y. Grosu, Effect of flexibility and nanotriboelectrification on the dynamic reversibility of water intrusion into nanopores: pressure-transmitting fluid with frequency-dependent dissipation capability, ACS Appl. Mater. Interfaces 11 (2019) 40842–40849, https://doi.org/10.1021/acsami.9b14031.
[17] L. Bartolomé, J.D. Littlefair, E. Amayuelas, L.J.W. Johnson, A. Le Donne, A. Šutka, S. Meloni, Y. Grosu, Triboelectrification during water Intrusion–Extrusion into-from hydrophobic nanopores, Adv. Mater. Technol. 10 (2025) 2401744, https://doi.org/10.1002/admt.202401744.
[18] L. Lapčinskis, K. Mālnieks, J. Blūms, M. Knite, S. Oras, T. Käämbre, S. Vlassov, M. Antsov, M. Timusk, A. Šutka, The Adhesion-Enhanced contact electrification and efficiency of triboelectric nanogenerators, Macromol. Mater. Eng. 305 (2020), https://doi.org/10.1002/mame.201900638.
[19] M.J. Sailor, Porous silicon in practice: preparation, Charact. Appl. (2012), https://doi.org/10.1002/9783527641901.
[20] M.P. Stewart, J.M. Buriak, Chemical and biological applications of porous silicon technology, Adv. Mater. 12 (2000) https://doi.org/10.1002/1521-4095(200006)12:12<859::AID-ADMA859>3.0.CO;2-0.
[21] A. Nattestad, A.J. Mozer, M.K.R. Fischer, Y.B. Cheng, A. Mishra, P. Bäuerle, U. Bach, Highly efficient photocathodes for dye-sensitized tandem solar cells, Nat. Mater. 9 (2010), https://doi.org/10.1038/nmat2588.
[22] M. Brinker, P. Huber, Wafer-Scale electroactive nanoporous silicon: large and fully reversible Electrochemo-Mechanical actuation in aqueous electrolytes, Adv. Mater. 34 (2022), https://doi.org/10.1002/adma.202105923.
[23] M. Brinker, P. Huber, A Mott-Schottky analysis of mesoporous silicon in aqueous electrolyte solution by electrochemical impedance spectroscopy, Electro Acta 483 (2024), https://doi.org/10.1016/j.electacta.2024.144038.
[24] S. Lin, M. Zheng, J. Luo, Z.L. Wang, Effects of surface functional groups on electron transfer at liquid–solid interfacial contact electrification, ACS Nano 14 (2020) 10733–10741, https://doi.org/10.1021/acsnano.0c06075.
[25] M. Sun, Q. Lu, Z.L. Wang, B. Huang, Understanding contact electrification at liquid–solid interfaces from surface electronic structure, Nat. Commun. 12 (2021) 1752, https://doi.org/10.1038/s41467-021-22005-6.
[26] S. Lin, M. Zheng, Z.L. Wang, Detecting the Liquid–Solid contact electrification charges in a liquid environment, J. Phys. Chem. C 125 (2021) 14098–14104, https://doi.org/10.1021/acs.jpcc.1c03483.
[27] D. Heo, J. Son, J. Hur, H. Yong, K. Cha, P.T.J. Hwang, B. Koo, Y. Gwak, Y. Jin, D. Kim, J. Hong, S. Lee, Ultra-High peak power generation for rotational triboelectric nanogenerator via simple charge control and boosted discharge design, Adv. Funct. Mater. 34 (2024) 2406032, https://doi.org/10.1002/adfm.202406032.
[28] S.H. Shin, Y.E. Bae, H.K. Moon, J. Kim, S.H. Choi, Y. Kim, H.J. Yoon, M.H. Lee, J. Nah, Formation of triboelectric series via Atomic-Level surface functionalization for triboelectric energy harvesting, ACS Nano 11 (2017), https://doi.org/10.1021/acsnano.7b02156.
[29] P.C. Griffiths, A. Paul, I.A. Fallis, C. Wellappili, D.M. Murphy, R. Jenkins, S. J. Waters, R. Nilmini, R.K. Heenan, S.M. King, Derivatizing weak polyelectrolytes-Solution properties, self-aggregation, and association with anionic surfaces of hydrophobically modified poly(ethylene imine), J. Colloid Interface Sci. 314 (2007), https://doi.org/10.1016/j.jcis.2007.05.082.
[30] I.C. Bellettini, L.G. Nandi, R. Eising, J.B. Domingos, V.G. Machado, E. Minatti, Properties of aqueous solutions of hydrophobically modified polyethylene imines in the absence and presence of sodium dodecylsulfate, J. Colloid Interface Sci. 370 (2012), https://doi.org/10.1016/j.jcis.2011.12.049.
[31] S.M. Kim, J. Ha, J.B. Kim, The effect of dielectric constant and work function on triboelectric nanogenerators: analytical and numerical study, Integr. Ferroelectr. 176 (2016), https://doi.org/10.1080/10584587.2016.1252657.
[32] X. Li, L. Zhang, Y. Feng, X. Zhang, D. Wang, F. Zhou, Solid–liquid triboelectrification control and antistatic materials design based on interface wettability control, Adv. Funct. Mater. 29 (2019), https://doi.org/10.1002/adfm.201903587.
[33] S. Li, J. Nie, Y. Shi, X. Tao, F. Wang, J. Tian, S. Lin, X. Chen, Z.L. Wang, Contributions of different functional groups to contact electrification of polymers, Adv. Mater. 32 (2020), https://doi.org/10.1002/adma.202001307.
[34] S. Bontapalle, A. Opitz, R. Schlesinger, S.R. Marder, S. Varughese, N. Koch, Electrode work function reduction by polyethylenimine interlayers: choice of solvent and residual solvent removal for superior functionality, Adv. Mater. Interfaces 7 (2020), https://doi.org/10.1002/admi.202000291.
[35] W. Tang, T. Jiang, F.R. Fan, A.F. Yu, C. Zhang, X. Cao, Z.L. Wang, Liquid-Metal electrode for High-Performance triboelectric nanogenerator at an instantaneous energy conversion efficiency of 70.6%, Adv. Funct. Mater. 25 (2015) 3718–3725, https://doi.org/10.1002/ADFM.201501331.
[36] X. Yang, S. Chan, L. Wang, W.A. Daoud, Water tank triboelectric nanogenerator for efficient harvesting of water wave energy over a broad frequency range, Nano Energy 44 (2018) 388–398, https://doi.org/10.1016/j.nanoen.2017.12.025.
[37] H. Wu, N. Mendel, S. van der Ham, L. Shui, G. Zhou, F. Mugele, Charge Trapping-Based electricity generator (CTEG): an ultrarobust and high efficiency nanogenerator for energy harvesting from water droplets, Adv. Mater. 32 (2020), https://doi.org/10.1002/adma.202001699.
[38] T. Liu, X. Cui, Z. Ye, X. Li, Y. Liu, B. Luo, S. Zhang, M. Chi, J. Wang, C. Cai, Y. Bai, S. Wang, S. Nie, A pulsed bubble-driven efficient liquid-solid triboelectric nanogenerator, Adv. Funct. Mater. 35 (2025) 2415483, https://doi.org/10.1002/adfm.202415483.
[39] V.A. Eroshenko, I. Piatiletov, L. Coiffard, V. Stoudenets, A new paradigm of mechanical energy dissipation. Part 2: experimental investigation and effectiveness of a novel car damper, Proc. Inst. Mech. Eng. Part D J. Automob. Eng. 221 (2007) 301–312, https://doi.org/10.1243/09544070D01605.
[40] R.F.W. Bader, Principle of stationary action and the definition of a proper open system, Phys. Rev. B 49 (1994), https://doi.org/10.1103/PhysRevB.49.13348.
[41] E. Sanville, S.D. Kenny, R. Smith, G. Henkelman, Improved grid-based algorithm for bader charge allocation, J. Comput. Chem. 28 (2007) 899–908, https://doi.org/10.1002/jcc.20575.
[42] D. Dollimore, P. Spooner, A. Turner, The bet method of analysis of gas adsorption data and its relevance to the calculation of surface areas, Surf. Technol. 4 (1976) 121–160, https://doi.org/10.1016/0376-4583(76)90024-8.
[43] J. Rouquerol, F. Rouquerol, P. Llewellyn, G. Maurin, K.S.W. Sing, Adsorption by Powders and Porous Solids, Elsevier, 2014, https://doi.org/10.1016/C2010-0-66232-8.
[44] J.B. Parra, J.C.De Sousa, R.C. Bansal, J.J. Pis, J.A. Pajares, Characterization of activated carbons by the BET equation – an alternative approach, Adsorpt. Sci. Technol. 12 (1995) 51–66, https://doi.org/10.1177/026361749501200106.
[45] E.P. Barrett, L.G. Joyner, P.P. Halenda, The determination of pore volume and area distributions in porous substances. I. computations from nitrogen isotherms, J. Am. Chem. Soc. 73 (1951), https://doi.org/10.1021/ja01145a126.
[46] S. Plimpton, Fast parallel algorithms for short-range molecular dynamics, J. Comput. Phys. 117 (1995) 1–19, https://doi.org/10.1006/jcph.1995.1039.
[47] A.P. Thompson, H.M. Aktulga, R. Berger, D.S. Bolintineanu, W.M. Brown, P. S. Crozier, P.J. in 't Veld, A. Kohlmeyer, S.G. Moore, T.D. Nguyen, R. Shan, M. J. Stevens, J. Tranchida, C. Trott, S.J. Plimpton, LAMMPS - a flexible simulation tool for particle-based materials modeling at the atomic, meso, and continuum scales, Comput. Phys. Commun. 271 (2022), https://doi.org/10.1016/j.cpc.2021.108171.
[48] F.S. Emami, V. Puddu, R.J. Berry, V. Varshney, S.V. Patwardhan, C.C. Perry, H. Heinz, Force field and a surface model database for silica to simulate interfacial properties in atomic resolution, Chem. Mater. 26 (2014) 2647–2658, https://doi.org/10.1021/cm500365c.
[49] S.W.I. Siu, K. Pluhackova, R.A. Böckmann, Optimization of the OPLS-AA force field for long hydrocarbons, J. Chem. Theory Comput. 8 (2012), https://doi.org/10.1021/ct200908r.
[50] J.L.F. Abascal, C. Vega, A general purpose model for the condensed phases of water: TIP4P/2005, J. Chem. Phys. 123 (2005) 234505, https://doi.org/10.1063/1.2121687.
[51] G. Kresse, J. Furthmüller, Efficiency of ab-initio total energy calculations for metals and semiconductors using a plane-wave basis set, Comput. Mater. Sci. 6 (1996), https://doi.org/10.1016/0927-0256(96)00008-0.
[52] G. Kresse, J. Furthmüller, Efficient iterative schemes for ab initio total-energy calculations using a plane-wave basis set, Phys. Rev. B Condens Matter Mater. Phys. 54 (1996), https://doi.org/10.1103/PhysRevB.54.11169.
[53] D. Joubert, From ultrasoft pseudopotentials to the projector augmented-wave method, Phys. Rev. B Condens Matter Mater. Phys. 59 (1999), https://doi.org/10.1103/PhysRevB.59.1758.
[54] G. Kresse, J. Hafner, Norm-conserving and ultrasoft pseudopotentials for first-row and transition elements, J. Phys. Condens. Matter 6 (1994), https://doi.org/10.1088/0953-8984/6/40/015.

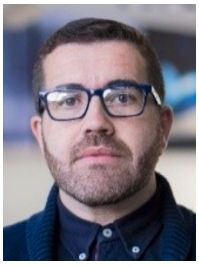

Dr. Luis Bartolomé is a physicist who earned his PhD in Mechanical Engineering and Materials from Mondragon University (Spain) in 2012. With a background in tribology, he combines academic and industrial experience, including postdoctoral research at the University of Ljubljana (Slovenia) and TU Delft (Netherlands), as well as a visiting researcher stay at the Polytechnic University of Catalonia (Spain). He is currently a senior researcher at CIC energiGUNE, working in the area of thermal energy storage and conversion. His research focuses on triboelectrification, solid–liquid interfaces, and nanostructured media to develop disruptive technologies for energy harvesting and thermal energy applications.

Dr. Nicola Verziaggi, born in 1999, earned his BSc in Chemistry *cum laude* in 2021, followed by an MSc in Chemical Sciences *cum laude* in 2023, both from the University of Ferrara (UNIFE), with a thesis on nickel-based catalysts for CO_2-free hydrogen production. Since November 2023, he has been a PhD student in computational chemistry, focusing on novel strategies for clean hydrogen production via methane thermal decomposition with a negative carbon footprint. His research exploits electronic structure calculations (DFT) and classical molecular dynamics. He contributed to the Horizon 2020 project 112CO2 and is currently involved in the Horizon 2020 Electro-Intrusion project.

Dr. Manuel Brinker is a physicist currently working as a post-doc at the Institute of Materials and X-Ray Physics at the Hamburg University of Technology under the supervision of Prof. Patrick Huber. Manuel's interest lies in porous materials, in particular porous silicon, with the main focus on their synthesis, and their electrochemical and mechanical features. In this field of research he obtained his Ph.D. in 2023.

Dr. Eder Amayuelas earned his Ph.D. in Materials Science from the University of the Basque Country in 2017, with a focus on the synthesis and structural characterization of porous materials such as metal-organic frameworks (MOFs). He is currently a postdoctoral researcher at CIC energiGUNE in the field of thermal energy storage and conversion. His research interests center on the development of advanced porous materials to address environmental and energy-related challenges, including pollutant removal, gas adsorption, and energy conversion. He places particular emphasis on understanding the structure-property relationships.

Dr. Sebastiano Merchiori obtained his MSc in Chemistry at the University of Ferrara (UNIFE) in 2019 with a thesis in Photochemistry. During his pre-doctoral years, he worked in various scientific fields: from Heat Transfer and PCMs for Thermal Energy Systems at the TekneHub laboratory to the synthesis of bio-based coatings for metals/alloys protection and studies on the corrosion behaviour of reinforced concrete at the Corrosion and Metallurgy Study Centre (UNIFE). He obtained his PhD cum laude in Inorganic Chemistry at UNIFE in 2025, conducting computational studies on {MOF+water} systems, with new findings on the behaviour of water under highly confined conditions.

Dr. Mesude Zeliha Arkan is an assistant professor in the Institute of Chemistry at the University of Silesia in Katowice, Poland. She received a BSc from the Department of Chemistry at Ege University (2011) and a master's degree in Energy from Ege University (2013). She obtained a Ph.D. degree from the Department of Materials Science and Engineering at Izmir Kâtip Çelebi University (2017). Her research interests include organic synthesis, self-assembled monolayers, surface modification, organic-inorganic hybrid structures, and their applications in device fabrication.

Dr. Raivis Eglītis completed his PhD in Materials Science in 2023 with a thesis on photochromic semiconductors. He is currently working as a researcher in the Institute of Physics and Materials Science at Riga Technical University. His research topics include triboelectric based on semiconductors as well as optically active semiconductors.

Prof. Andris Šutka received his Ph.D. in chemical engineering sciences in 2012 at Riga Technical University (RTU) in Latvia. After obtaining his Ph.D., he executed post-doctoral research in Estonia at the University of Tartu (2013–2016). Currently, he is a tenure-track Professor at the RTU, in the Institute of Physics and Materials Sciences, Faculty of Natural Sciences and Technology. He is leading a research group that includes 15 members on different research topics, including triboelectric and soft piezoelectric materials, decoupled water electrolysis, electrocatalysis, Smart Window materials for energy management, gas sensor materials, and antibacterial coatings.

Prof. Mirosław Chorążewski is the group leader of the Thermodynamics in Action Team at the University of Silesia in Katowice, which is a multidisciplinary group of experienced instrumentalists. His research interests are high-pressure calorimetry, thermodynamics, equations of states, and solid-liquid interfaces. In 2009, he was a post-doc at the Eduard Hála Laboratory of Thermodynamics Academy of Sciences of the Czech Republic, where he worked together with Professor Ivan Wichterle on a project involving high-pressure fluid phase equilibria. In 2006 and 2009–2011, he worked as a post-doc at the University of Blaise Pascal (France), where he worked with Professor Jean-Pierre Grolier on the thermodynamic modeling of high-pressure properties of compressed liquids, including fuels.

Prof. Patrick Huber earned his Ph.D. in physics from Saarland University in 1999, followed by a research fellowship at Harvard University, where he studied liquid metals using synchrotron X-ray scattering. He habilitated in 2008 and held academic positions at Saarland University and the Pontifical Catholic University of Chile in Santiago. He has been a visiting scientist at the Max Planck Institute in Potsdam and a visiting professor in Lyon, France. He currently leads a research group at DESY and is head of the Institute for Materials and X-Ray Physics at TUHH.

Prof. Simone Meloni is a Professor of Inorganic Chemistry at the University of Ferrara. His research bridges molecular simulation, thermodynamics, and materials science, with a focus on energy conversion, nanoconfined fluids, and reactive systems. He has made significant contributions to understanding phase behavior and transport phenomena in complex environments, including nanoporous materials. Prof. Meloni combines atomistic modeling with theoretical approaches to unravel structure–property relationships at the nanoscale, e.g., the fundamental principles of triboelectrification. He actively collaborates with experimentalists to guide the design of novel energy materials. His work has been published in leading journals and recognized with national and international awards.

Prof. Yaroslav Grosu is a group leader of the Interfacial Phenomena and Porous Media group at CIC energiGUNE research center. He is also a Professor at the University of Silesia (Poland) and an Honorary Professor of Surface Science and Energy Materials Engineering at the University of Birmingham (UK). His research focuses on energy storage and conversion, with expertise in solid-liquid interfaces, nanoporous materials, nanofluids, and corrosion. He earned a cotutelle PhD from Blaise Pascal University (France) and the National Technical University of Ukraine and has conducted research at University of California Davis (USA), University of Birmingham, International Iberian Nanotechnology Laboratory (Portugal).